



Large enhancement of magnetocaloric effect induced by dual regulation effects of hydrostatic pressure in $\text{Mn}_{0.94}\text{Fe}_{0.06}\text{NiGe}$ compound

He Zhou^{a,1}, Dekun Wang^{a,1}, Zhe Li^b, Junzhuang Cong^c, Ziyuan Yu^a, Shuo Zhao^a, Peng Jiang^a, Daoyong Cong^d, Xinqi Zheng^a, Kaiming Qiao^a, Hu Zhang^{a,*}

^a School of Materials Science and Engineering, University of Science and Technology Beijing, Beijing 100083, China

^b College of Physics and Electronic Engineering, Key Laboratory for Advanced Functional and Low Dimensional Materials of Yunnan Higher Education Institute, Qujing Normal University, Qujing 655011, China

^c MultiFields Technologies (Beijing) Co. Ltd., Beijing 100190, China

^d State Key Laboratory for Advanced Metals and Materials, University of Science and Technology Beijing, Beijing 100083, China

ARTICLE INFO

Article history:

Received 28 June 2021

Revised 14 November 2021

Accepted 22 November 2021

Available online 15 January 2022

Keywords:

Magnetocaloric effect

Magnetostructural transition

Hydrostatic pressure

Magnetic properties

ABSTRACT

$\text{MM}'\text{X}$ (M , M' = transition metals, X = carbon or boron group elements) compounds could exhibit large magnetocaloric effect due to the magnetostructural transition, and the composition regulation has been widely studied to realize the magnetostructural transition. Moreover, the magnetostructural transition is also sensitive to the pressure. Herein, the effect of hydrostatic pressure on magnetostructural transformation and magnetocaloric effect has been investigated in $\text{Mn}_{0.94}\text{Fe}_{0.06}\text{NiGe}$ compound. Dual regulation effect of lowering structural transition temperature and strengthening ferromagnetic (FM) state of martensite is realized by applying hydrostatic pressure, which would greatly improve the magnetocaloric effect of $\text{Mn}_{0.94}\text{Fe}_{0.06}\text{NiGe}$ compound. Moreover, the first-principles calculations have also been performed to discuss the origin of the regulation effect under hydrostatic pressure, and it indicates that the hydrostatic pressure can stabilize the hexagonal structure and decrease the structural transition temperature. The maximum isothermal entropy change increases by 109% from 4.3 J/(kg K) under 0 GPa to 9.0 J/(kg K) under 0.402 GPa for a magnetic field change of 0–3 T. This work proves that the hydrostatic pressure is an effective method to regulate the magnetostructural transition and enhance magnetocaloric effect in $\text{MM}'\text{X}$ compounds.

© 2022 Published by Elsevier Ltd on behalf of The editorial office of Journal of Materials Science & Technology.

1. Introduction

Magnetic materials that experience magnetostructural transition usually exhibit various magnetoresponsive effects, such as magnetoresistance [1], magnetocaloric effect (MCE) [2,3], magnetostriction [4,5] and Hall effect [6]. As one of the typical materials with magnetostructural transition, $\text{MM}'\text{X}$ (M , M' = transition metals, X = carbon or boron group elements) compounds have been reported to present considerable MCE around room temperature [7–9], which makes $\text{MM}'\text{X}$ compounds the potential candidates for room temperature magnetic refrigeration materials.

Among the $\text{MM}'\text{X}$ system, the stoichiometric MnNiGe undergoes a structural transition at 470 K from the high-temperature

Ni_2In -type hexagonal structure (space group $\text{P6}_3/\text{mmc}$, 194) to the low-temperature TiNiSi -type orthorhombic structure (space group Pnma , 62) [10,11]. Since this structural transition temperature (T_{str}) is much higher than the magnetic transition temperature ($T_{\text{N}}^{\text{M}} = 346$ K) of orthorhombic phase, magnetostructural transition cannot be obtained in the stoichiometric MnNiGe compound [12]. Therefore, many efforts have been made to regulate the structural and magnetic transition temperatures in order to realize the magnetostructural transition [13–15].

For $\text{MM}'\text{X}$ compounds, composition regulation is the most commonly used method to tune the magnetostructural transition. The substitution and vacancy of transition metals and main group elements could affect the structural transition temperature and magnetic properties of $\text{MM}'\text{X}$ compounds and then obtain the desired magnetostructural transition [16–21]. For example, substituting Fe for Mn or Ni in MnNiGe can give rise to a significant reduction of T_{str} . Moreover, substituting Fe for Mn can introduce ferromagnetic

* Corresponding author.

E-mail address: zhanghu@ustb.edu.cn (H. Zhang).

¹ These authors contributed equally to this work.

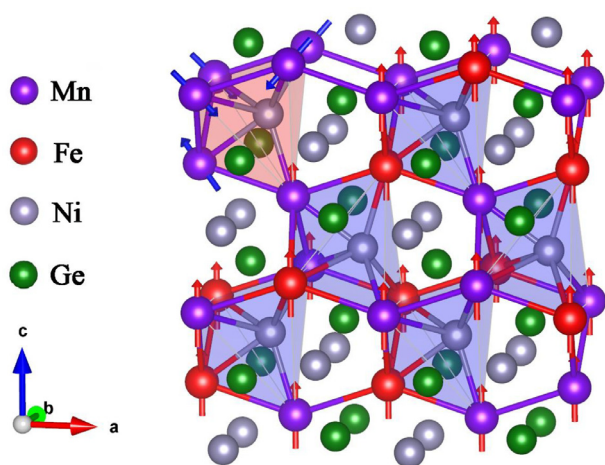


Fig. 1. TiNiSi-type orthorhombic crystal structure of $\text{Mn}_{1-x}\text{Fe}_x\text{NiGe}$ compounds with indicated Ni-6Mn local configurations (light pink zone) and Ni-6Mn/Fe local configurations (light blue zone). The arrows on Mn and Fe atoms illustrate the magnetic moments.

(FM) coupling between Fe and Mn atoms and break up the consecutive antiferromagnetic (AFM) sublattices of the Mn moments [12], as shown in Fig. 1, thus prompting the magnetic state of martensite to transform from spiral AFM to FM states. This would then lead to a magnetostructural transition from a paramagnetic (PM) hexagonal phase to a FM orthorhombic phase [12,22]. Furthermore, the first-principles calculations reveal that the AFM-FM conversion is originated from the shrinkage of Mn-Mn distance [23]. In addition, the structural transition is also sensitive to the hydrostatic pressure, and a pressure-induced enhancement of the MCE has been observed in some compounds with magnetostructural transition [24–26]. The effect of hydrostatic pressure has been investigated in some $\text{MM}'\text{X}$ compounds [13,27–32]. The hydrostatic pressure can stabilize the hexagonal phase and push the T_{str} to the lower temperature due to the shortening of Mn-Mn distance, thus leading to the decoupling of magnetostructural transition as well as the reduction of MCE [27,30]. However, in comparison with the research on composition regulation, in-depth work on pressure regulation may be worthwhile to further obtain the regulation mechanism.

According to the phase diagram [12], $\text{Mn}_{0.94}\text{Fe}_{0.06}\text{NiGe}$ is around the phase boundary of Fe content = 0.08 between AFM and FM states, and so it exhibits a weak AFM magnetostructural transition due to the appearance of FM configurations. This intermediate state suggests that the magnetic structure of this composition might be easily tuned by hydrostatic pressure. With this in mind, the effect of hydrostatic pressure on the magnetostructural transition and MCE of $\text{Mn}_{0.94}\text{Fe}_{0.06}\text{NiGe}$ has been studied in present work. The application of hydrostatic pressure results in the dual regulation effects, i.e., lowering the T_{str} and strengthening the FM state, thus leading to the large enhancement of MCE in $\text{Mn}_{0.94}\text{Fe}_{0.06}\text{NiGe}$ compound. In addition, the effect of pressure on T_{str} is analyzed by the first-principles calculations.

2. Experimental and theoretical methods

The $\text{Mn}_{0.94}\text{Fe}_{0.06}\text{NiGe}$ compound was prepared by arc-melting the pure components on a water-cooled copper hearth under argon atmosphere. The as-cast sample was annealed in a high-vacuum quartz tube at 1123 K for five days, and then cooled slowly to room temperature to avoid stress in the sample. The temperature-dependent powder X-ray diffraction (XRD) measurements were performed by using Bruker D8-Advance diffractometer with $\text{Cu K}\alpha$

radiation. The Rietveld refinement based on the XRD patterns was carried out to identify the crystal structure and lattice parameters using the LHPM Rietica software [33]. The differential scanning calorimetry (DSC) measurements were carried out using DSC 6220 with a heating/cooling rate of 10 K/min. The magnetization was measured using a vibrating sample magnetometer (VSM, Versalab, Quantum Design) equipped with the copper beryllium clamp type pressure cell. The pressure inside the cell was calibrated by the shifts of the Curie temperature of Gd, which is put together with the specimen during measurements. The applied pressure can be determined based on the corresponding relationship between Curie temperature of Gd and pressure [34].

The first-principles calculations were carried out using the Vienna *ab initio* simulation package (VASP, version: 6.1.1) based on the density-functional theory (DFT) [35]. The electronic exchange-correlation energies were treated using the generalized gradient approximation (GGA) and the Perdew-Burke-Ernzerhof (PBE) [36]. The interactions between atomic core and valence electrons are described by the projected-augmented wave (PAW) pseudopotential [37]. The following valence electron configurations of atoms were used: $3d^6 4s^1$ for Mn, $3d^6 4s^2$ for Fe, $3d^8 4s^1$ for Ni, and $4s^2 4p^2$ for Ge. The calculated convergence precision of each atom was set at 1×10^{-5} eV, and the energy cutoff was set to 450 eV to ensure higher accuracy. A $9 \times 9 \times 7$ Monkhorst-Pack *k*-point mesh was used in the first Brillouin region for the hexagonal supercell, and a $4 \times 7 \times 7$ meshes was used for the orthorhombic supercell. The method of first-order Methfessel-Paxton with 0.2 eV as the width of smearing was used for the geometry optimization of the models [38]. The unit cell parameters and volume were optimized for the hexagonal supercell, while only unit cell volume was optimized for the orthorhombic supercell to prevent atoms from leaving the idealized positions.

3. Results and discussion

Fig. 2(a) shows the XRD patterns of $\text{Mn}_{0.94}\text{Fe}_{0.06}\text{NiGe}$ measured at different temperatures in a heating mode. $\text{Mn}_{0.94}\text{Fe}_{0.06}\text{NiGe}$ crystallizes in a single phase with orthorhombic structure at low temperatures. With increasing temperature, the diffraction peaks of hexagonal structure start to appear at 260 K and become stronger gradually, indicating the structural transformation from orthorhombic structure to hexagonal structure. The $\text{Mn}_{0.94}\text{Fe}_{0.06}\text{NiGe}$ becomes the pure hexagonal phase when the temperature is higher than 360 K. Fig. 2(b) shows the Rietveld refined XRD pattern of $\text{Mn}_{0.94}\text{Fe}_{0.06}\text{NiGe}$ at 300 K. The coexistence of ~63.6 wt.% hexagonal phase and ~36.4 wt.% orthorhombic phase confirms that the T_{str} is around room temperature. For $\text{MM}'\text{X}$ compounds, the TiNiSi-type structure can be regarded as an orthorhombic distortion of the Ni_2In -type hexagonal structure. The axes and volumes of the orthorhombic and hexagonal structures are related as $a_o = c_h$, $b_o = a_h$, $c_o = 3a_h$ and $V_o = 2V_h$ [12]. It clearly indicates that the unit cell volume of the orthorhombic phase is twice that of the hexagonal phase. Therefore, it is necessary to compare $V_{\text{orth}}/2$ with V_{hex} in order to understand the unit cell volume change during the structural transition. As shown in the inset of Fig. 2(b), the unit cell volume increases by ~2.67% ($\Delta V/V = (V_{\text{orth}}/2 - V_{\text{hex}})/V_{\text{hex}}$) during the structural transition from hexagonal to orthorhombic phases, indicating that the $\text{Mn}_{0.94}\text{Fe}_{0.06}\text{NiGe}$ compound experiences a large negative thermal expansion through the structural transition from hexagonal structure to orthorhombic structure. Moreover, the cell volume of $\text{Mn}_{0.94}\text{Fe}_{0.06}\text{NiGe}$ is also smaller than that of stoichiometric MnNiGe [10]. This suggests the Mn-Mn distance becomes smaller with the Fe doping, which would strengthen the FM state in $\text{Mn}_{0.94}\text{Fe}_{0.06}\text{NiGe}$. Fig. 2(c) shows the DSC heat flow curves in zero field for $\text{Mn}_{0.94}\text{Fe}_{0.06}\text{NiGe}$. The large endothermic and exother-

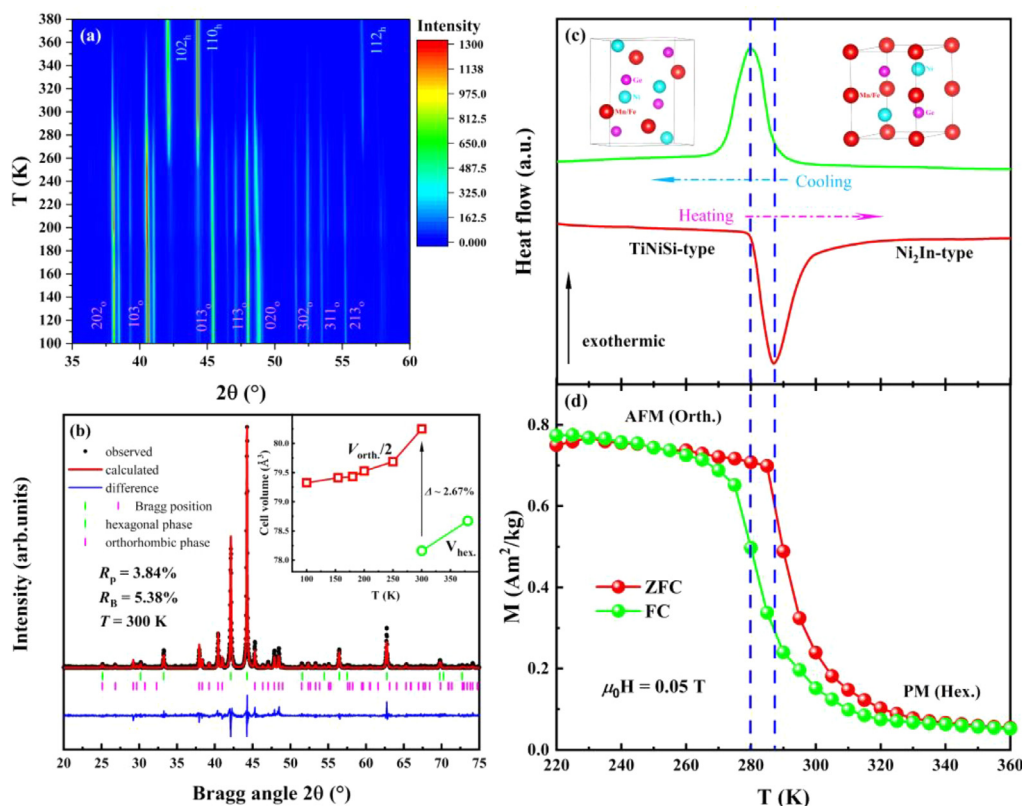


Fig. 2. (a) The contour plot of temperature dependent of the XRD patterns for $\text{Mn}_{0.94}\text{Fe}_{0.06}\text{NiGe}$ compound. (b) The observed and refined powder XRD patterns of $\text{Mn}_{0.94}\text{Fe}_{0.06}\text{NiGe}$ compound at 300 K. The inset shows the unit cell volume as a function of temperature. (c) DSC heat flow curves for $\text{Mn}_{0.94}\text{Fe}_{0.06}\text{NiGe}$ compound. (d) The temperature dependences of ZFC and FC magnetizations under 0.05 T for $\text{Mn}_{0.94}\text{Fe}_{0.06}\text{NiGe}$ compound.

mic DSC peaks with distinct thermal hysteresis during the heating and cooling processes indicate the first-order structural transition between the Ni_2In -type structure and TiNiSi -type structure. Based on the DSC data, the entropy change (ΔS_{str}) can be estimated to be 42.5 J/(kg K) (the averaged value of those measured on cooling and heating) by using the equation $\Delta S_{\text{str}} = \int_{T_1}^{T_2} \frac{1}{T} \frac{Q}{T'} dT$, where Q is the heat flux and T' is the scanning rate. The large ΔS_{str} value indicates a strong first-order magnetostructural transition, in line with other MM'X compounds with similar TiNiSi to Ni_2In transitions [22,39]. In addition, the T_{str} is estimated to be 280 K ($T_{\text{str}}^{\text{cooling}}$) and 287 K ($T_{\text{str}}^{\text{heating}}$) for $\text{Mn}_{0.94}\text{Fe}_{0.06}\text{NiGe}$, which is significantly lower than the $T_{\text{str}} = 470$ K of stoichiometric MnNiGe . This result implies that the substitution of Fe for Mn in MnNiGe could stabilize the hexagonal phase and push T_{str} towards lower temperatures. The temperature (T) dependences of zero-field-cooling (ZFC) and field-cooling (FC) magnetizations (M) under 0.05 T for $\text{Mn}_{0.94}\text{Fe}_{0.06}\text{NiGe}$ are displayed in Fig. 2(d). $\text{Mn}_{0.94}\text{Fe}_{0.06}\text{NiGe}$ undergoes a magnetic transition with distinct thermal hysteresis, and the magnetic transition temperatures determined from M - T curves are consistent with the structural transition temperatures obtained from DSC curves. This result implies that $\text{Mn}_{0.94}\text{Fe}_{0.06}\text{NiGe}$ might experience a magnetostructural transformation between PM hexagonal phase and FM-like orthorhombic phase. However, the magnetization of orthorhombic phase in $\text{Mn}_{0.94}\text{Fe}_{0.06}\text{NiGe}$ is still much lower than those of other FM Fe-doped MnNiGe compounds. Considering the Fe content of 0.06 is still lower than the phase boundary point of 0.08 [12], we assume that the orthorhombic phase of $\text{Mn}_{0.94}\text{Fe}_{0.06}\text{NiGe}$ is still in AFM state, which can be further confirmed by the M - $\mu_0 H$ measurements. Moreover, as mentioned above, the substitution of Mn by Fe in MnNiGe could promote the magnetic state of orthorhom-

bic phase to transform from AFM to FM states [12,22]. Since the $\text{Mn}_{0.94}\text{Fe}_{0.06}\text{NiGe}$ is near the phase boundary between AFM and FM states based on phase diagram, the AFM state of orthorhombic phase in present compound would be weakened by the competition of introduced FM coupling. Therefore, the hydrostatic pressure could more easily drive the weakened AFM state to FM state.

Fig. 3(a) shows the temperature dependences of ZFC and FC magnetizations under 0.05 T for $\text{Mn}_{0.94}\text{Fe}_{0.06}\text{NiGe}$ at various applied hydrostatic pressures. The T_{str} shifts largely to the lower temperatures with increasing pressure. This result suggests that hydrostatic pressure could shorten the Mn-Mn distance, which then stabilizes the hexagonal phase and reduces T_{str} to the lower temperatures [27,29]. The inset of Fig. 3(a) plots the transition temperatures as a function of pressure. The T_{str} decreases almost linearly with the application of pressure as a rate of -32 K/GPa. This value is in reasonable agreement with the shift of transition temperature $dT_{\text{str}}/dP \approx -39.3$ K/GPa estimated from the Clausius-Clapeyron equation $dT_{\text{str}}/dP = \Delta V/\Delta S_{\text{str}}$, with a volume change of $\Delta V \approx -1.67$ mm³/g (Fig. 2(b)) and $\Delta S_{\text{str}} \approx 42.5$ J/(kg K). Such a large rate implies that hydrostatic pressure could be an effective method to tune the T_{str} . In addition, the thermal hysteresis increases from 5 K under 0 GPa to 7 K under 0.402 GPa. This reveals that hydrostatic pressure could strengthen the nature of first-order magnetostructural transition by lowering the T_{str} further into the temperature window of magnetostructural coupling. Furthermore, another change of magnetization can be observed around 200 K. According to the neutron diffraction study [10], this variation of magnetization may be attributed to the change in modulation axis of the incommensurate AFM ordering, i.e., the spiral axis changes from being in the bc -plane to along the a -axis. Moreover, the applied pressure can drive the magnetization change around 200 K to higher temperature. It can be seen from Fig. 2(b)

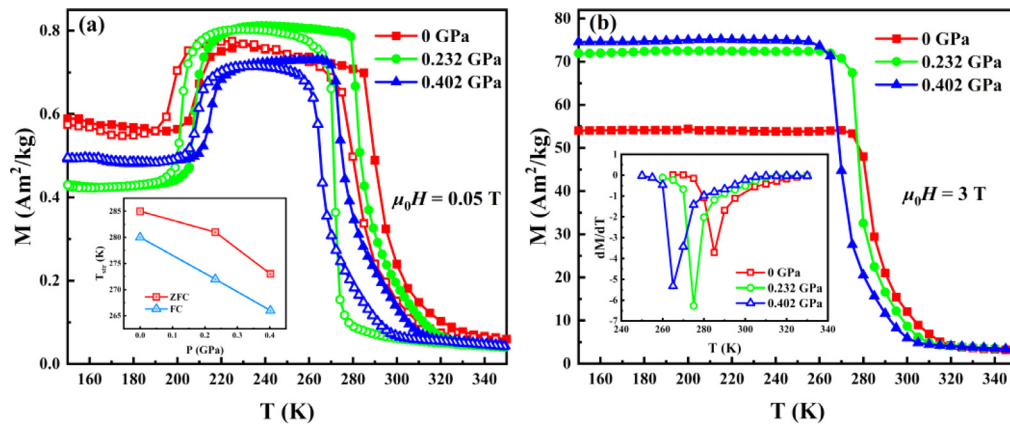


Fig. 3. (a) The temperature dependences of ZFC (solid symbol) and FC (open symbol) magnetizations under 0.05 T for $\text{Mn}_{0.94}\text{Fe}_{0.06}\text{NiGe}$ compound at different applied pressures. The inset shows the T_{str} as a function of pressure for $\text{Mn}_{0.94}\text{Fe}_{0.06}\text{NiGe}$ compound. (b) The temperature dependences of FC magnetizations under 3 T for $\text{Mn}_{0.94}\text{Fe}_{0.06}\text{NiGe}$ compound at various applied pressures. The inset shows the dM/dT as a function of temperature.

that the cell volume of orthorhombic phase increases with the increase of temperature around 200 K, indicating that the change in modulation axis from bc -plane to a -axis leads to the lattice expansion. According to the Le Chatelier's Principle, the increase in external pressure will displace the equilibrium to favor the phase with the lower volume. Therefore, the pressure will stabilize the low-temperature incommensurate AFM ordering with the lower volume, thus shifting the change in modulation axis towards higher temperature, as presently observed on the magnetization under pressure in Fig. 3(a). The temperature dependences of magnetizations under 3 T for $\text{Mn}_{0.94}\text{Fe}_{0.06}\text{NiGe}$ at different applied pressures are shown in Fig. 3(b). The magnetization change around 200 K vanishes under a high magnetic field of 3 T, indicating that the applied magnetic field can tilt the balance between the AFM and FM competition and induce the AFM-FM transition of orthorhombic phase. Therefore, the magnetization change around 200 K is gradually suppressed with increasing field. Moreover, the magnetization of orthorhombic phase in $\text{Mn}_{0.94}\text{Fe}_{0.06}\text{NiGe}$ under pressure is distinctly higher than that under 0 GPa. This implies the possible presence of field-induced transition from AFM to FM states under pressure, which can be also confirmed by the following M - $\mu_0 H$ study. The inset of Fig. 3(b) shows the corresponding dM/dT versus T curves under different pressures. The T_{str} gradually decreases with increasing the applied pressure, which is consistent with the above results. In addition, the magnetostructural transition is significantly broadened under $P = 0.402$ GPa, and transition temperature span increases from 40 K under 0 GPa to 55 K under 0.402 GPa. Similar results can be found in other MM'/X compounds under hydrostatic pressure, and the broadening of the transition under pressure can be ascribed to the decoupling of magnetic and structural transitions [27,40].

Fig. 4 shows the magnetization isotherms of $\text{Mn}_{0.94}\text{Fe}_{0.06}\text{NiGe}$ with magnetizing and demagnetizing processes under (a) 0 GPa and (b) 0.402 GPa, respectively. The isothermal magnetization (M - $\mu_0 H$) curves were measured by adopting a loop process method to eliminate the residual effect [8,41]. The sample was heated up to complete PM state and then cooled back to the target temperature under zero field before each isothermal magnetization measurement. As shown in Fig. 4(a), the magnetization of $\text{Mn}_{0.94}\text{Fe}_{0.06}\text{NiGe}$ increases slowly with increasing magnetic field, confirming that it exhibits an AFM state at low temperatures. A slight magnetic hysteresis is observed around the transition temperature, proving the first-order magnetostructural transition from the AFM orthorhombic phase to the PM hexagonal phase. In addition, a small jump of magnetization occurs around the T_{str} above the critical field ($\mu_0 H_{\text{cr}}$) of ~ 2.7 T, implying that AFM components can be in-

duced into FM components under a higher field. With the application of pressure, it is seen from Fig. 4(b) that the magnetic hysteresis increases while the $\mu_0 H_{\text{cr}}$ decreases largely. This confirms that hydrostatic pressure could strengthen the first-order magnetostructural transition and promote the conversion from AFM to FM states. In order to further study the effect of pressure on magnetic property, the magnetization isotherms of $\text{Mn}_{0.94}\text{Fe}_{0.06}\text{NiGe}$ at 260 K under different applied pressures are plotted in Fig. 4(c). Under the same field, the magnetization increases remarkably with the increase of pressure, further proving that hydrostatic pressure is favorable for the formation of FM components. Moreover, $\text{Mn}_{0.94}\text{Fe}_{0.06}\text{NiGe}$ under 0 GPa does not show a field-induced metamagnetic transition at 260 K even under the high field of 3 T. In contrast, it shows a field-induced metamagnetic transition from AFM to FM states with increasing pressure, which further enhances the magnetization in comparison with that under 0 GPa. For example, the M value is about $73.6 \text{ Am}^2/\text{kg}$ under 3 T under 0.402 GPa, which is about 47% higher than the M of $50.1 \text{ Am}^2/\text{kg}$ without applied pressure. It is seen from the inset of Fig. 4(c) that the $\mu_0 H_{\text{cr}}$ decreases linearly at a rate of 2 T/GPa. The reduction of $\mu_0 H_{\text{cr}}$ with applied pressure is beneficial for obtaining a FM magnetostructural transition as well as large MCE under lower magnetic fields.

The DFT calculations were carried out to further understand the influence of applied pressure on structural transformation. In order to simulate the doping with a small amount of Fe, a $2 \times 2 \times 2$ supercell of the hexagonal phase and a $2 \times 2 \times 1$ supercell of the orthorhombic phase were constructed, and one of the symmetry-independent Mn atoms in each structure was replaced with a Fe atom. This model corresponds to a doping ratio of 6.25% ($\text{Mn}_{0.9375}\text{Fe}_{0.0625}\text{NiGe}$), which is close to the experimental composition. The crystalline structures of hexagonal and orthorhombic supercells are shown in Fig. 5(a) and (b), respectively. In the Ni_2In -type hexagonal structure, according to the atomic occupancy rule dominated by covalent electron numbers [42], Mn and Fe atoms occupy $2a$ sites, Ni atoms occupy $2d$ sites, and Ge atoms occupy $2c$ sites. After the non-diffusion and displacement martensitic transformation, all atoms still occupy their relatively unchanged sites in the TiNiSi -type orthorhombic structure [12,43]. The geometry optimizations were carried out for both non-spin-polarized (NSP) and spin-polarized (SP) models. The total energies and unit cell parameters of the optimized structural models are listed in Table 1. Considering the calculation error of ~ 1 meV/atom, it can be found that the spin polarization would reduce the total energy of the system for both hexagonal and orthorhombic structures. Therefore, the spin-polarized structure is the ground state structure under the condition of temperature (T) = 0 and pressure (P) = 0 for

Table 1

Calculated lattice parameters, cell volume (V) and total energy (E_{tot}) of the optimized structural models for the hexagonal and orthorhombic structures of $\text{Mn}_{0.9375}\text{Fe}_{0.0625}\text{NiGe}$.

Structure	Model	Lattice parameters (Å)			V (Å ³)	E_{tot} (eV/atom)
		a	b	c		
Hexagonal	NSP	8.130	8.130	9.984	571.565	−6.350
	SP	8.173	8.173	10.503	607.592	−6.524
Orthorhombic	NSP	11.810	7.296	6.912	595.642	−6.282
	SP	12.036	7.435	7.045	630.455	−6.526

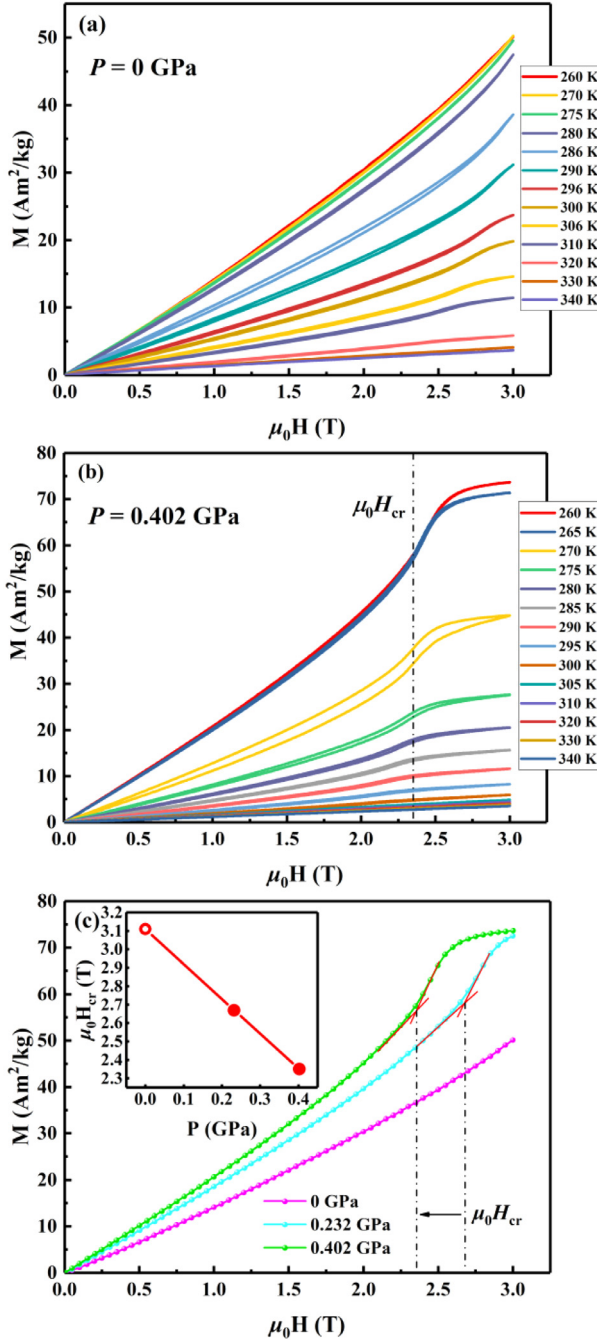


Fig. 4. Magnetization isotherms with magnetizing and demagnetizing processes for $\text{Mn}_{0.94}\text{Fe}_{0.06}\text{NiGe}$ compound under (a) 0 GPa and (b) 0.402 GPa. (c) The magnetization isotherms of $\text{Mn}_{0.94}\text{Fe}_{0.06}\text{NiGe}$ compound under different applied pressures at 260 K. The inset shows the $\mu_0 H_{\text{cr}}$ as a function of pressure for $\text{Mn}_{0.94}\text{Fe}_{0.06}\text{NiGe}$ compound.

hexagonal and orthorhombic phases. Moreover, the spin-polarized orthorhombic structure is the most stable structure from the perspective of the total energy of the system.

Fig. 5(c) shows the total and the partial densities of state (DOS) of orthorhombic structure for $\text{Mn}_{0.9375}\text{Fe}_{0.0625}\text{NiGe}$. Only d -electron DOS and p -electron DOS are given for $3d$ and p -block elements, respectively. It can be found that the majority spin DOS mainly locates below the Fermi level (E_F) and the minority spin DOS locates above the E_F for Mn $3d$ state, which leads to a large spin splitting in majority and minority spin channels at the E_F . This would make a large magnetic moment on Mn atom ($\sim 3.02 \mu_B$). In addition, the $3d$ state of Fe shows a great similarity of DOS distribution as the Mn $3d$ state, but the minority spin channels below E_F are slightly more occupied than those of Mn $3d$ state. Thus, the Fe atom carries a smaller magnetic moment ($\sim 2.28 \mu_B$) due to the relatively weak spin splitting. On the contrary, the Ni and Ge atoms carry very small moments as the spin polarizations are very weak due to the strong covalent bonds between Ni and Ge atoms. As a result, the Mn/Fe atoms carry the main magnetic moments and mostly dominate the magnetic properties, which is in a good agreement with previous reports [9,44].

It is well known that the crystal structure with the lowest energy is the preferred structure by nature. The Gibbs free energy (G) can be expressed as [45]

$$G(P, T) = E_{\text{coh}} + PV - TS - MB \quad (1)$$

where E_{coh} is the cohesive energy, V is the unit cell volume, S is the entropy, M is the magnetization, and B is the magnetic field. As the present DFT calculations cannot reproduce the application of a magnetic field, the MB term is neglected. Similar approximations can be also found in other works which led to reasonable results on the effect of pressure [46,47]. The cohesive energy can be defined as the energy required to separate a crystal structure into single atoms, and the total energy of the system obtained by DFT calculation can be regarded as the cohesive energy [45]. The structural transition between two phases with different crystal structures can be predicted by calculating the Gibbs free energy change (ΔG) between two structures, which can be calculated by the following equation [45]:

$$\Delta G(P, T) = \Delta E_{\text{coh}} + P\Delta V - T\Delta S \quad (2)$$

For solid-state materials, the first two terms tend to be much larger than the entropic contribution from the last term in this expression, so the last term of ΔG can be safely neglected [48]. As a result, the Gibbs free energy change can be simplified as

$$\Delta G(P, T) \cong \Delta E_{\text{coh}} + P\Delta V \quad (3)$$

In DFT calculations, all analyzes are based on the idea that the crystal structure is always in the lowest Gibbs free energy, which implies that the Gibbs free energy can be considered to remain approximately unchanged under the condition of $T = 0$ [45]. Therefore, the pressure can be defined by

$$P = -\frac{\partial E_{\text{coh}}}{\partial V} \quad (4)$$

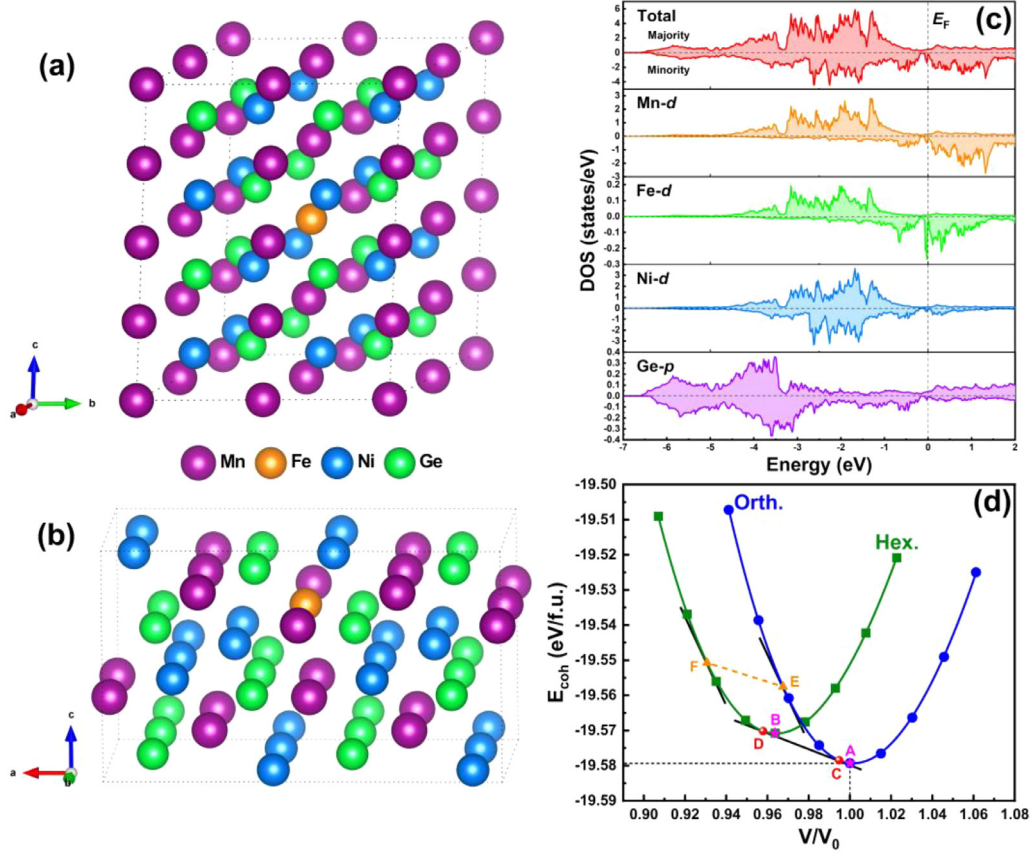


Fig. 5. The crystal structures of (a) hexagonal supercell and (b) orthorhombic supercell for $\text{Mn}_{0.9375}\text{Fe}_{0.0625}\text{NiGe}$. (c) The total and partial DOS of orthorhombic structure. (d) The E_{coh} as a function of V/V_0 for hexagonal and orthorhombic structures.

The change of cohesive energy with volume can be obtained by the DFT calculation. The FM orthorhombic structure is used as the preferred crystal structure at the ground state ($P = 0$ and $T = 0$) for the calculations. Fig. 5(d) shows the unit cell volume compressibility (V/V_0) dependence of E_{coh} for hexagonal and orthorhombic structures, where V_0 is the unit cell volume of orthorhombic structure in the ground state. It can be found that the change of E_{coh} with V/V_0 can be well fitted on the basis of the Birch-Murnaghan equation [48,49]:

$$E_{\text{coh}}(V) = E_0 + \frac{9V_0B_0}{16} \left\{ \left[\left(\frac{V_0}{V} \right)^{\frac{2}{3}} - 1 \right]^3 B'_0 \left[\left(\frac{V_0}{V} \right)^{\frac{2}{3}} - 1 \right]^2 \left[6 - 4 \left(\frac{V_0}{V} \right)^{\frac{2}{3}} \right] \right\} \quad (5)$$

where E_0 is the E_{coh} of orthorhombic structure at $P = 0$, B_0 is the bulk modulus, and B'_0 is the derivative of the bulk modulus with respect to pressure. According to Eq. (4), the slope (α) of any point on the $E_{\text{coh}}-V/V_0$ curves can be expressed as

$$\alpha = \frac{\partial E_{\text{coh}}}{\partial (V/V_0)} = V_0 \frac{\partial E_{\text{coh}}}{\partial V} = -V_0 P \quad (6)$$

Therefore, the pressure that is relevant for any point on the $E_{\text{coh}}-V/V_0$ curves can be defined by

$$P = -\frac{\alpha}{V_0} \quad (7)$$

Accordingly, the same α implies the same pressure for hexagonal and orthorhombic structures. Moreover, based on Eqs. (3) and (7), the Gibbs free energy change between hexagonal and orthorhombic

structures can be expressed as follows:

$$\begin{aligned} \Delta G_{\text{hex.-orth.}} &= \Delta E_{\text{hex.-orth.}} + P \Delta V_{\text{hex.-orth.}} \\ &= E_{\text{hex.}} - E_{\text{orth.}} - \frac{\alpha}{V_0} (V_{\text{hex.}} - V_{\text{orth.}}) \end{aligned} \quad (8)$$

As shown in Fig. 5(d), the lowest points (points A and B) of the $E_{\text{coh}}-V/V_0$ curves represent the state of $P = 0$. According to Eq. (8), the Gibbs free energy change between hexagonal and orthorhombic phases at $P = 0$ can be expressed as

$$\Delta G_{\text{hex.-orth.}} = E_{\text{hex.}} - E_{\text{orth.}} > 0 \quad (9)$$

which indicates that the orthorhombic phase has lower Gibbs free energy at $P = 0$. The point lower than the lowest V/V_0 value suggests the reduction of V , which is equivalent to the application of a pressure on the material. It can be found that the E_{coh} goes up with increasing pressure for both hexagonal and orthorhombic structures. The curve for orthorhombic structure shares a common tangent with the curve for hexagonal structure at the points C and D, i.e., the slope α is same at both C and D points. According to Eq. (7), this fact implies that the hexagonal and orthorhombic structures have same pressure at points C and D. The α at points C and D on the $E_{\text{coh}}-V/V_0$ curves can be expressed as

$$\alpha = \frac{E_{\text{orth.}} - E_{\text{hex.}}}{V_{\text{orth.}} - V_{\text{hex.}}} V_0 \quad (10)$$

Substituting Eq. (10) into Eq. (8), the Gibbs free energy change between hexagonal and orthorhombic structures can be obtained as follows:

$$\Delta G_{\text{hex.-orth.}} = E_{\text{hex.}} - E_{\text{orth.}} - \frac{E_{\text{orth.}} - E_{\text{hex.}}}{V_{\text{orth.}} - V_{\text{hex.}}} (V_{\text{hex.}} - V_{\text{orth.}}) = 0 \quad (11)$$

That is, $G_{\text{hex.}} = G_{\text{orth.}}$. This result proves that the hexagonal and orthorhombic structures would have the same Gibbs free energy at

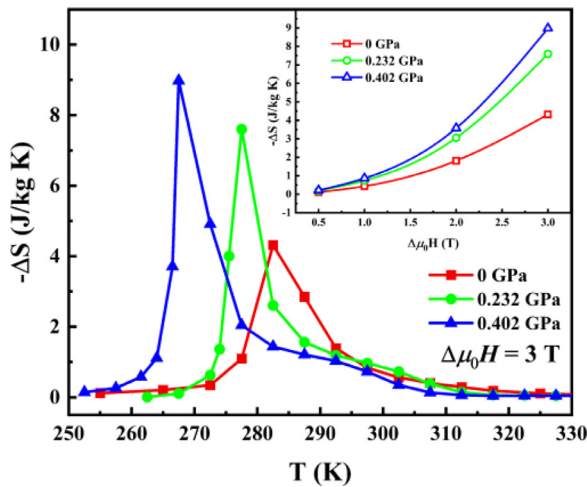


Fig. 6. Temperature dependences of $-\Delta S$ under a field change of 0–3 T for $\text{Mn}_{0.94}\text{Fe}_{0.06}\text{NiGe}$ compound under different applied pressures. The inset shows the magnetic field dependences of maximum $-\Delta S$ value for $\text{Mn}_{0.94}\text{Fe}_{0.06}\text{NiGe}$ compound under different applied pressures.

points C and D, and it also falls back on the standard expression, that is, $\Delta G_{\text{phase1}} = \Delta G_{\text{phase2}}$ at a first order transition point between two phases. With further increasing pressure, such as the pressure corresponding to points E and F in Fig. 5(d), the α at points E and F meets

$$\alpha < \frac{E_{\text{orth.}} - E_{\text{hex.}}}{V_{\text{orth.}} - V_{\text{hex.}}} V_0 \quad (12)$$

Substituting Eq. (12) into Eq. (8), it can be inferred that $\Delta G_{\text{hex.}-\text{orth.}} < 0$, indicating that the Gibbs free energy of hexagonal structure is lower than that of orthorhombic structure under larger pressure. Consequently, above result indicates that the pressure favors to stabilize the hexagonal phase and induce the structural transformation from orthorhombic to hexagonal structures, thus reducing the structural transition temperature. Moreover, this result is in line with the sign of the dT_{str}/dP estimated from Clausius-Clapeyron formalism ($dT_{\text{str}}/dP \approx -39.3$ K/GPa). In addition, according to the Le Chatelier's Principle, the applied pressure will stabilize the hexagonal phase with lower volume, thus decreasing the structural transition temperature, which is consistent with the above results.

The isothermal entropy change (ΔS) were calculated from the $M-\mu_0 H$ curves by using the Maxwell relation [50]:

$$\Delta S(T, H) = \mu_0 \int_0^H \left(\frac{\partial M}{\partial T} \right)_H dH \quad (13)$$

Fig. 6 shows the temperature dependences of $-\Delta S$ under a magnetic field change of 0–3 T for $\text{Mn}_{0.94}\text{Fe}_{0.06}\text{NiGe}$ under different applied pressures. The T_{str} decreases while the $-\Delta S$ increases largely with increasing pressure. In addition to the $-\Delta S$ peak at 267 K, another small $-\Delta S$ bump is also observed around 285 K for the compound under 0.402 GPa. The broadening of the high temperature wing of the ΔS peak should originate from the tail of the broadened transition under pressure. The inset of Fig. 6 plots the maximum $-\Delta S$ value as a function of magnetic field for $\text{Mn}_{0.94}\text{Fe}_{0.06}\text{NiGe}$ under different applied pressures. The maximum $-\Delta S$ is enhanced remarkably by the applied pressure, especially when the field is higher than 2 T. For a field change of 0–3 T, the maximum $-\Delta S$ of 9.0 J/(kg K) under 0.402 GPa is 109% higher than the maximum $-\Delta S$ of 4.3 J/(kg K) without pressure. The maximum $-\Delta S$ of 4.3 J/(kg K) under ambient pressure is much lower than the entropy change ($\Delta S_{\text{str}} = 42.5$ J/(kg K)) calculated from DSC. The entropy change obtained from DSC corresponds to the total

entropy change during the complete transition [51]. Therefore, the lower isothermal entropy change ΔS suggests that the magnetic field of 3 T cannot induce the complete phase transition at $P = 0$. But, the application of an external pressure appears to promote an increase in the fraction of ΔS_{str} being involved in ΔS . In addition, the strengthening of FM coupling and increased magnetization induced by the pressure also increases the entropy change, especially above the critical field (>2 T) of field-induced metamagnetic transition, as shown in the inset of Fig. 6. Consequently, the present result reveals that the hydrostatic pressure can significantly enhance the MCE of $\text{Mn}_{0.94}\text{Fe}_{0.06}\text{NiGe}$ by dual regulation effects, i.e., increasing the entropy change by lowering the T_{str} further into the temperature window of magnetostructural coupling as well as by strengthening the FM state.

4. Conclusion

In conclusion, the hydrostatic pressure could shorten the Mn–Mn distance in $\text{Mn}_{0.94}\text{Fe}_{0.06}\text{NiGe}$, which then stabilizes the hexagonal phase and lowers the T_{str} further into the temperature window of magnetostructural coupling. Moreover, the hydrostatic pressure could also strengthen the FM state of orthorhombic phase and facilitate the conversion from AFM to FM states. The decrease of T_{str} caused by hydrostatic pressure is also confirmed by the first-principles calculations. These dual regulation effects of hydrostatic pressure enhance the MCE largely. The maximum $-\Delta S$ value increases significantly from 4.3 J/(kg K) under 0 GPa to 9.0 J/(kg K) under 0.402 GPa. This work proves that the hydrostatic pressure is an effective method to regulate the magnetostructural transition and enhance MCE in MM'X compounds.

Declaration of Competing Interest

The authors declare that they have no known competing financial interests or personal relationships that could have appeared to influence the work reported in this paper.

Acknowledgments

This work was financially supported by the National Key Research and Development Program of China (No. 2017YFB0702704), the National Natural Science Foundation of China (No. 51671022), the State Key Lab of Advanced Metals and Materials (No. 2019-Z11), the Fundamental Research Funds for the Central Universities (No. FRF-TP-18-014B1) and the Youth Teacher International Exchange & Growth Program (No. QNXM20210014).

References

- [1] S. Singh, R. Rawat, S.E. Muthu, S.W. D'Souza, E. Suard, A. Senyshyn, S. Banik, P. Rajput, S. Bhardwaj, A.M. Awasthi, R. Ranjan, S. Arumugam, D.L. Schlager, T.A. Lograsso, A. Chakrabarti, S.R. Barman, Phys. Rev. Lett. 109 (2012) 246601.
- [2] A. Biswas, A.K. Pathak, N.A. Zarkevich, X.B. Liu, Y. Mudryk, V. Balema, D.D. Johnson, V.K. Pecharsky, Acta Mater 180 (2019) 341–348.
- [3] J. Liu, T. Gottschall, K.P. Skokov, J.D. Moore, O. Gutfleisch, Nat. Mater. 11 (2012) 620–626.
- [4] C.L. Zhang, H.F. Shi, Y.G. Nie, E.J. Ye, J.H. Wen, Z.D. Han, D.H. Wang, J. Alloy. Compd. 784 (2019) 16–21.
- [5] J. Liu, Y.Y. Gong, F.Q. Zhang, Y.R. You, G.Z. Xu, X.F. Miao, F. Xu, J. Mater. Sci. Technol. 76 (2021) 104–110.
- [6] I. Dubenko, A.K. Pathak, S. Stadler, N. Ali, Y. Kovarskii, V.N. Prudnikov, N.S. Perov, A.B. Granovsky, Phys. Rev. B 80 (2009) 092408.
- [7] N.T. Trung, L. Zhang, L. Caron, K.H.J. Buschow, E. Brück, Appl. Phys. Lett. 96 (2010) 172504.
- [8] Y.W. Li, H. Zhang, K. Tao, Y.X. Wang, M.L. Wu, Y. Long, Mater. Des. 114 (2017) 410–415.
- [9] Z.Y. Wei, E.K. Liu, Y. Li, G.Z. Xu, X.M. Zhang, G.D. Liu, X.K. Xi, H.W. Zhang, W.H. Wang, G.H. Wu, X.X. Zhang, Adv. Electron. Mater. 1 (2015) 1500076.
- [10] W. Bažela, A. Szytuła, J. Todorović, Z. Tomkowicz, A. Zieba, Phys. Stat. Sol. A 38 (1976) 721–729.
- [11] W. Bažela, A. Szytuła, J. Todorović, A. Zieba, Phys. Stat. Sol. A 64 (1981) 367–378.

- [12] E.K. Liu, W.H. Wang, L. Feng, W. Zhu, G.J. Li, J.L. Chen, H.W. Zhang, G.H. Wu, C.B. Jiang, H.B. Xu, F. de Boer, *Nat. Commun.* 3 (2012) 873.
- [13] A. Taubel, T. Gottschall, M. Fries, T. Faske, K.P. Skokov, O. Gutfleisch, *J. Phys. D Appl. Phys.* 50 (2017) 464005.
- [14] E.K. Liu, H.G. Zhang, G.Z. Xu, X.M. Zhang, R.S. Ma, W.H. Wang, J.L. Chen, H.W. Zhang, G.H. Wu, L. Feng, X.X. Zhang, *Appl. Phys. Lett.* 102 (2013) 122405.
- [15] J. Liu, Y.Y. Gong, Y.R. You, X.M. You, B.W. Huang, X.F. Miao, G.Z. Xu, F. Xu, E. Brück, *Acta Mater.* 174 (2019) 450–458.
- [16] A. Aryal, A. Quetz, S. Pandey, T. Samanta, I. Dubenko, M. Hill, D. Mazumdar, S. Stadler, N. Ali, *J. Alloy. Compd.* 709 (2017) 142–146.
- [17] A. Aryal, A. Quetz, C.F. Sánchez-Valdés, P.J. Ibarra-Gaytán, S. Pandey, I. Dubenko, J.L.S. Llamazares, S. Stadler, N. Ali, *Intermetallics* 97 (2018) 89–94.
- [18] J.H. Chen, A. Trigg, T. Poudel Chhetri, D.P. Young, I. Dubenko, N. Ali, S. Stadler, *J. Appl. Phys.* 127 (2020) 213901.
- [19] C.L. Zhang, Z.D. Han, B. Qian, H.F. Shi, C. Zhu, J. Chen, T.Z. Wang, *J. Appl. Phys.* 114 (2013) 153907.
- [20] C.L. Zhang, D.H. Wang, Q.Q. Cao, Z.D. Han, H.C. Xuan, Y.W. Du, *Appl. Phys. Lett.* 93 (2008) 122505.
- [21] A. Aryal, S. Bakkar, H. Samassekou, S. Pandey, I. Dubenko, S. Stadler, N. Ali, D. Mazumdar, *J. Alloy. Compd.* 823 (2020) 153770.
- [22] K. Xu, Z. Li, E.K. Liu, H.C. Zhou, Y.L. Zhang, C. Jing, *Sci. Rep.* 7 (2017) 41675.
- [23] S.C. Ma, K. Liu, C.C. Ma, Q. Ge, J.T. Zhang, Y.F. Hu, E.K. Liu, Z.C. Zhong, *Appl. Phys. Lett.* 111 (2017) 232404.
- [24] L. Morellon, Z. Arnold, C. Magen, C. Ritter, O. Prokhnenko, Y. Skorokhod, P.A. Algarabel, M.R. Ibarra, J. Kamarad, *Phys. Rev. Lett.* 93 (2004) 137201.
- [25] T. Samanta, D.L. Lepkowski, A.U. Saleheen, A. Shankar, J. Prestigiacomo, I. Dubenko, A. Quetz, I.W.H. Oswald, G.T. McCandless, J.Y. Chan, P.W. Adams, D.P. Young, N. Ali, S. Stadler, *Phys. Rev. B* 91 (2015) 020401R.
- [26] V.K. Sharma, M.K. Chattopadhyay, S.B. Roy, *J. Phys. Condens. Matter* 23 (2011) 366001.
- [27] P. Dutta, S. Pramanick, D. Das, S. Chatterjee, *J. Phys. D Appl. Phys.* 49 (2016) 385001.
- [28] L. Caron, N.T. Trung, E. Brück, *Phys. Rev. B* 84 (2011) 020414.
- [29] R.R. Wu, L.F. Bao, F.X. Hu, H. Wu, Q.Z. Huang, J. Wang, X.L. Dong, G.N. Li, J.R. Sun, F.R. Shen, T.Y. Zhao, X.Q. Zheng, L.C. Wang, Y. Liu, W.L. Zuo, Y.Y. Zhao, M. Zhang, X.C. Wang, C.Q. Jin, G.H. Rao, X.F. Han, B.G. Shen, *Sci. Rep.* 5 (2015) 18027.
- [30] Q.Q. Zeng, J.L. Shen, E.K. Liu, X.K. Xi, W.H. Wang, G.H. Wu, X.X. Zhang, *Chin. Phys. Lett.* 37 (2020) 076101.
- [31] S. Anzai, K. Ozawa, *Phys. Rev. B* 18 (1978) 2173–2178.
- [32] F.R. Shen, H.B. Zhou, F.X. Hu, J.T. Wang, H. Wu, Q.Z. Huang, J.Z. Hao, Z.B. Yu, Y.H. Gao, Y. Lin, Y.X. Wang, C. Zhang, Z. Yin, J. Wang, S.H. Deng, J. Chen, L.H. He, T.J. Liang, J.R. Sun, T.Y. Zhao, B.G. Shen, *J. Am. Chem. Soc.* 143 (2021) 6798–6804.
- [33] B.A. Hunter, Rietica, in a visual rietveld program, international union of crystallography commission on powder diffraction newsletter, 20 (1998) 21.
- [34] M. Mito, K. Matsumoto, Y. Komorida, H. Deguchi, S. Takagi, T. Tajiri, T. Iwamoto, T. Kawae, M. Tokita, K. Takeda, *J. Phys. Chem. Solids* 70 (2009) 1290–1296.
- [35] J. Hafner, *Comput. Phys. Commun.* 177 (2007) 6–13.
- [36] J.P. Perdew, K. Burke, M. Ernzerhof, *Phys. Rev. Lett.* 77 (1996) 3865–3868.
- [37] G. Kresse, D. Joubert, *Phys. Rev. B* 59 (1999) 1758–1775.
- [38] M. Methfessel, A.T. Paxton, *Phys. Rev. B* 40 (1989) 3616–3621.
- [39] A. Aznar, P. Lloveras, J.Y. Kim, E. Stern-Taulats, M. Barrio, J.L. Tamarit, C.F. Sanchez-Valdes, J.L. Sanchez Llamazares, N.D. Mathur, X. Moya, *Adv. Mater.* 31 (2019) 1903577.
- [40] F.X. Liang, F.R. Shen, Y. Liu, J. Li, K.M. Qiao, J. Wang, F.X. Hu, J.R. Sun, B.G. Shen, *AIP Adv.* 8 (2018) 056417.
- [41] L. Caron, Z.Q. Ou, T.T. Nguyen, D.T. Cam Thanh, O. Tegus, E. Brück, *J. Magn. Magn. Mater.* 321 (2009) 3559–3566.
- [42] A. Szytula, A.T. Pedziwiatr, Z. Tomkowicz, W. Bažela, *J. Magn. Magn. Mater.* 25 (1981) 176–186.
- [43] Y.N. Xiao, H. Zhang, Y.L. Zhang, K.W. Long, C.F. Xing, Y.W. Liu, Y. Long, *J. Alloy. Compd.* 769 (2018) 916–921.
- [44] Y. Li, Z.Y. Wei, E.K. Liu, G.D. Liu, S.G. Wang, W.H. Wang, G.H. Wu, *J. Appl. Phys.* 117 (2015) 17C117.
- [45] D.S. Sholl, J.A. Steckel, *Density Functional Theory: A Practical Introduction*, John Wiley & Sons, Hoboken, New Jersey, 2009.
- [46] K.R. Hahn, E. Assaf, A. Portavoce, S. Bertaina, A. Charaï, *J. Phys. Chem. C* 121 (2017) 26575–26586.
- [47] A. Paul, A. Mukherjee, I. Dasgupta, A. Paramekanti, T. Saha-Dasgupta, *Phys. Rev. Lett.* 122 (2019) 016404.
- [48] R. Dronskowski, *Computational Chemistry of Solid State Materials: A Guide For Materials Scientists, Chemists, Physicists and Others*, Wiley-VCH Verlag GmbH & Co. KGaA, Weinheim, Germany, 2005.
- [49] F. Birch, *Phys. Rev.* 71 (1947) 809–824.
- [50] V.K. Pecharsky, K.A. Gschneidner, *J. Appl. Phys.* 86 (1999) 565–575.
- [51] L. Mañosa, D. González-Alonso, A. Planes, E. Bonnot, M. Barrio, J.L. Tamarit, S. Aksoy, M. Acet, *Nat. Mater.* 9 (2010) 478–481.